VLA line observations of OH/IR stars

Herman, J.; Baud, B.; Habing, H.J.; Winnberg, A.

Astron. Astrophys. 143, 122–135 (1985)

ASTRONOMY AND ASTROPHYSICS

VLA line observations of OH/IR stars

J. Herman [1,*], B. Baud [2], H.J. Habing [1], and A. Winnberg [3]

[1] Sterrewacht Leiden, Postbus 9513, NL-2300 RA Leiden, The Netherlands
[2] Laboratorium voor Ruimteonderzoek, Postbus 800, NL-9700 AV Groningen, The Netherlands
[3] Onsala Space Observatory, S-439 00 Onsala, Sweden

Received June 20, accepted September 4, 1984

Summary. We used the VLA in a spectral line mode at 1612 MHz to investigate the structure of eleven OH/IR stars. Ten objects have large radial velocities and are expected to be close to their tangential points. For six resolved sources very accurate distances could be derived by combining the angular radii of the OH shell with available phase lag diameters. A comparison of these geometric distances with kinematic distances gives a determination of the distance to the Galactic Centre of 9.2 ± 1.2 kpc. The OH shells appear to be fairly symmetric, with deviations from spherical symmetry of less than 20%, and rather thin, the thickness being at most 20% of the radius. The OH density falls off as r^{-2}, or slightly steeper.

Key words: stars: long period variables – stars: OH/IR – circumstellar shells – interferometry – OH masers – galactic centre: distance

1. Introduction

The last stages of stellar evolution, in the red giant region of the Hertzsprung Russell diagram, have become an increasingly frequent subject of observational and theoretical studies ever since the infrared and microwave parts of the spectrum became accessible. Most objects in the 2.2 μm InfraRed Catalogue (IRC; Neugebauer and Leighton, 1969) are late-type giants (see e.g. Bidelman, 1980). The detection of maser emission from molecules such as OH, H_2O, and SiO in these objects (see Engels' catalogue, 1979) was one of the milestones and ultimately led to the discovery of an extreme class of red giants and supergiants: the OH/IR stars (see e.g. Jones et al., 1983; Herman and Habing, 1984b).

The OH/IR stars characteristically have spectra at $\lambda = 18$ cm which are dominated by two peaks with a separation of 20–40 $\mathrm{km\,s^{-1}}$ with steep outer edges, and a more gradual decline between these peaks. This shape of the spectrum can be explained if the maser emission comes from a rather thin, uniformly expanding shell (Reid et al., 1977). In this picture the strongest maser emission originates from the front and from the back sides of the shell. The separation between the outer peaks is twice the expansion velocity, v_e, of the shell; the stellar velocity, v_*, lies halfway between the peaks.

In this paper the OH emission structure of a sample of eleven OH/IR stars at large distances is studied with the VLA [1]. Because the stars are at the distance of the tangential point, where the line of sight is closest to the Galactic Centre, these measurements allow us for the first time to make an independent estimate of the galactic distance scale.

In the past decade the spatial structure of OH shells around late-type stars has been studied by using VLBI [2] techniques (e.g. Masheder et al., 1977; Benson and Mutel, 1979; Bowers et al., 1980). Extremely small emission spots were found with very high brightness temperatures ($T_B > 10^9$ K), that confirmed the presence of natural masers. But in the VLBI measurements only a small fraction of the total flux could be detected and the results neither contradicted, nor confirmed the suggested expanding shell geometry. However, not until observations with intermediate baselines became available (Booth et al., using MERLIN [3]), was such a geometry found. By making maps at different velocities, i.e. at different depths along the line of sight (see Baud, 1981; using the VLA), one may study the 3-dimensional structure of the envelope. That allows us to verify the expanding shell geometry, to find the radii of the OH shells, and to determine the density distribution. Most of the OH/IR stars appear to be (very) long period variables, and since 1978 sixty of them were monitored with the Dwingeloo Radio Telescope (Herman and Habing, 1984a). By combining "phase lag" radii, derived from the light travel times between the front and the back sides of the shells, with the angular extents it is possible to determine distances to the individual objects with high accuracy.

2. Observations and reduction

We used the VLA in New Mexico in the A-configuration on February 28 and March 1, 1982, to observe eleven OH/IR stars (see Thompson et al., 1980 for a general description of the VLA). Ten of these sources have large radial velocities, selected because (a) they were thought to be close to the tangential points, thus not having

Send offprint requests to: J. Herman
* Present address: ESTEC, Postbus 299, 2200 AG Noordwijk ZH, The Netherlands

1 Very Large Array of the National Radio Astronomy Observatory (NRAO). The NRAO is operated by Associated Universities, Inc., under contract with the National Science Foundation
2 Very Long Baseline Interferometry
3 Multi Element Radio Linked Interferometer Network

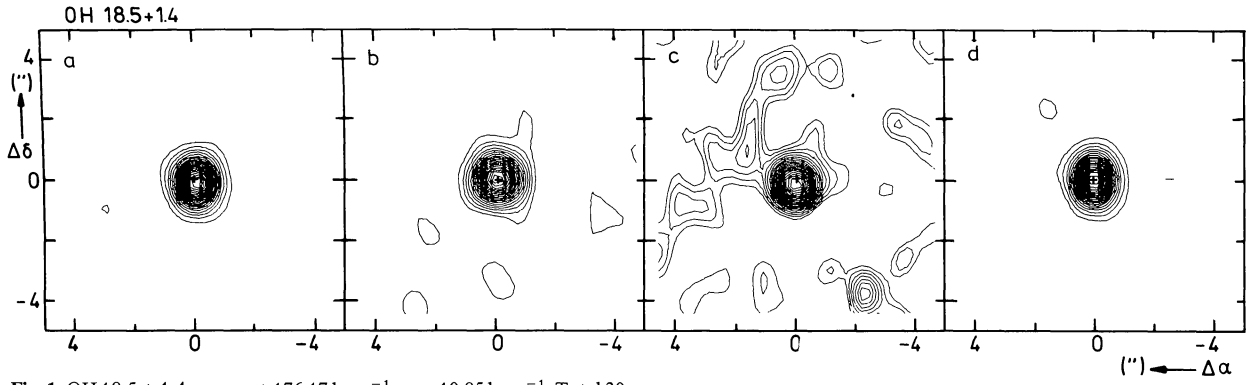

Fig. 1. OH 18.5 + 1.4, $v_{LSR} = +176.17\,km\,s^{-1}$, $v_e = 10.85\,km\,s^{-1}$, Total 30 maps

Map	Velocity ($km\,s^{-1}$)	Strongest peak (Jy)	Map	Velocity ($km\,s^{-1}$)	Strongest peak (Jy)
a	10.73	4.1	c	− 4.19	0.3
b	6.72	1.2	d	− 9.93	6.0

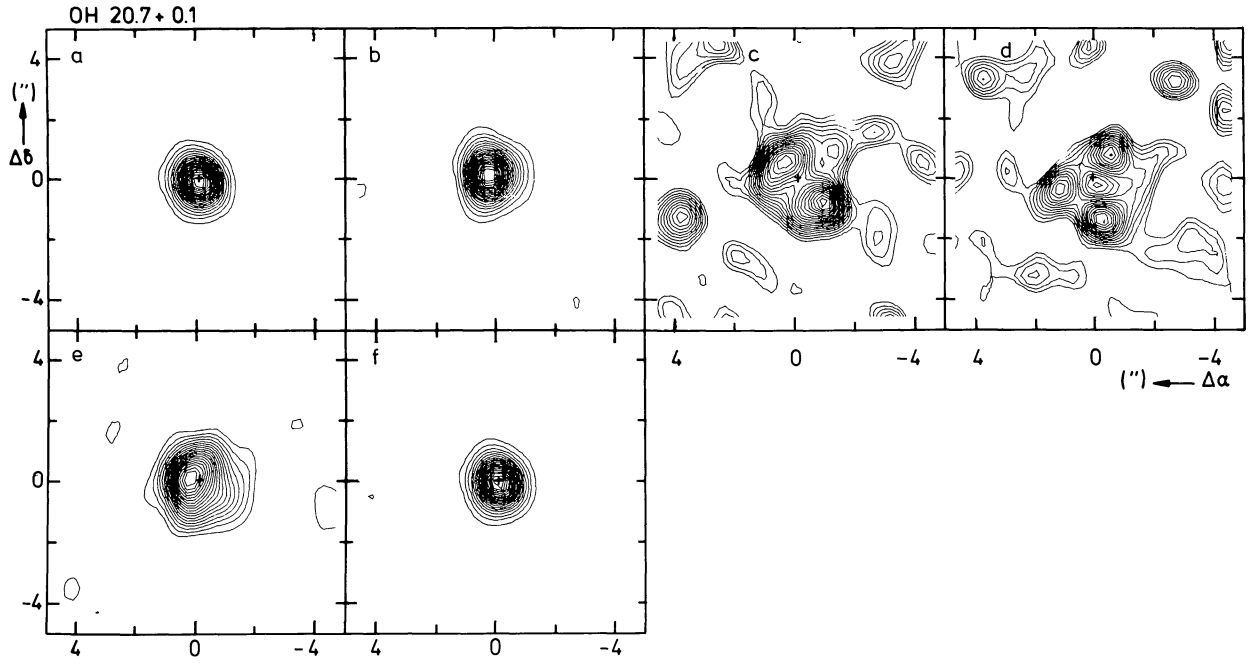

Fig. 2. OH 20.7 + 0.1, $v_{LSR} = +136.55\,km\,s^{-1}$, $v_e = 18.21\,km\,s^{-1}$, Total 20 maps

Map	Velocity ($km\,s^{-1}$)	Strongest peak (Jy)	Map	Velocity ($km\,s^{-1}$)	Strongest peak (Jy)
a	18.31	4.2	d[a]	− 6.08	0.5
b	16.02	2.4	e	−14.98	0.9
c[a]	5.40	0.06	f	−18.43	9.2

[a] c and d are the mean over $10.9\,km\,s^{-1}$

the kinematic distance ambiguity; (b) we had good positions for them; and (c) they were in the Dwingeloo monitor program. As a check on our procedures we included OH 26.5 + 0.6, which had been observed before (Baud, 1981). Six of our objects have small expansion velocities of the circumstellar shell ($v_e < 15\,km\,s^{-1}$) and five have large ones ($v_e > 15\,km\,s^{-1}$). All sources were observed in four short cuts of 10–15 min each, separated over 1.5 hours, except for OH 26.5 + 0.6, which was observed only once ($t_{int} = 5$ min). Calibration measurements were made every 20 min on the continuum source 1741–038 (1.972 ± 0.012 Jy on 28-2-82, based on 13.830 Jy for 3C286 at 1612 MHz).

On the first day we observed the sources with small expansion velocities. With 13 telescopes, a bandwidth of 197 kHz, 64 frequency (=velocity) channels, and a Hanning smoothed resolution of 6.2 kHz ($1.2\,km\,s^{-1}$), a rms noise $N \simeq 0.03$ Jy per channel was obtained after 50 min integration time. The largest

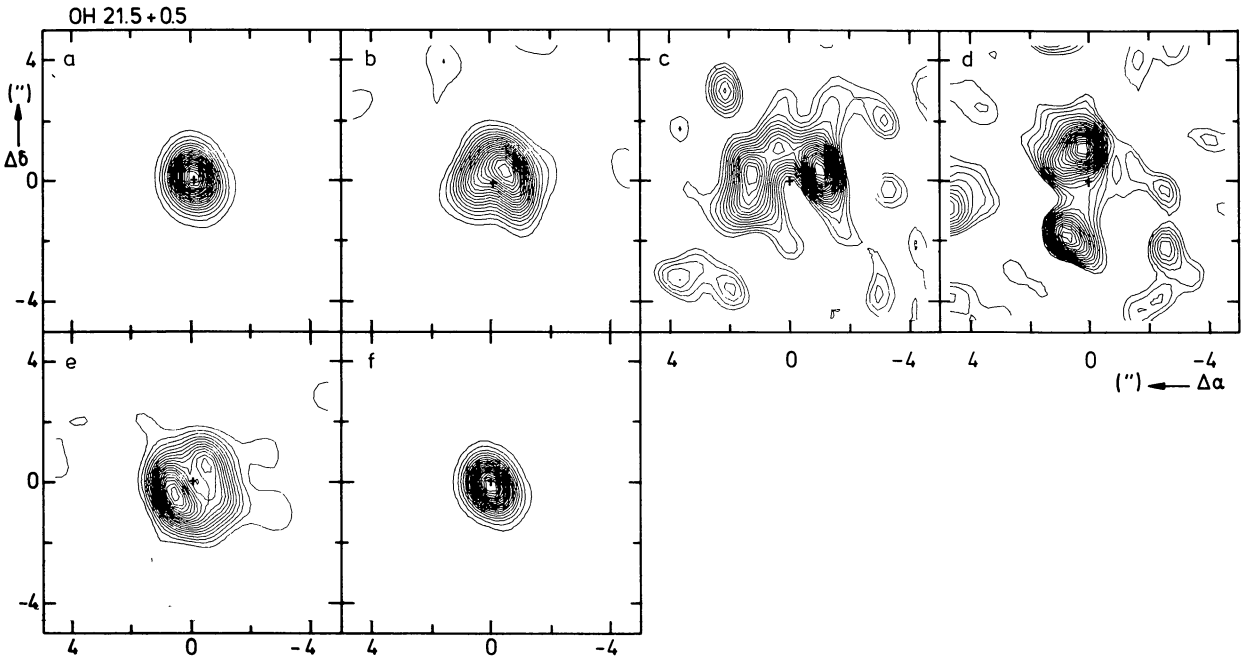

Fig. 3. OH 21.5 + 0.5, $v_{LSR} = +115.77\,km\,s^{-1}$, $v_e = 18.76\,km\,s^{-1}$, Total 21 maps

Map	Velocity ($km\,s^{-1}$)	Strongest peak (Jy)	Map	Velocity ($km\,s^{-1}$)	Strongest peak (Jy)
a	18.60	8.2	d[a]	− 4.94	0.06
b	16.88	0.9	e[a]	−13.55	0.47
c[a]	7.69	0.07	f	−18.71	7.1

[a] c is the mean over $14.9\,km\,s^{-1}$; d is the mean over $9.2\,km\,s^{-1}$; e is the mean over $2.3\,km\,s^{-1}$

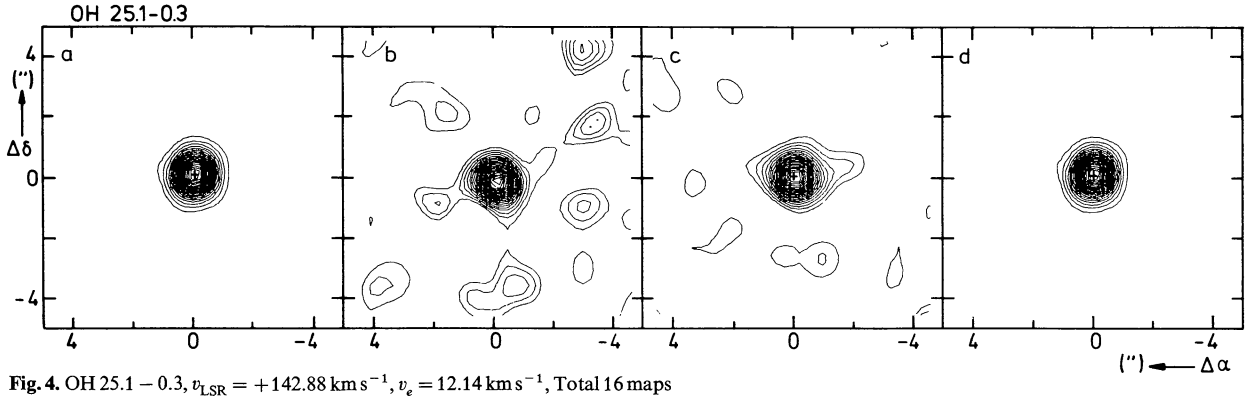

Fig. 4. OH 25.1 − 0.3, $v_{LSR} = +142.88\,km\,s^{-1}$, $v_e = 12.14\,km\,s^{-1}$, Total 16 maps

Map	Velocity ($km\,s^{-1}$)	Strongest peak (Jy)	Map	Velocity ($km\,s^{-1}$)	Strongest peak (Jy)
a	12.23	4.4	c[a]	− 9.30	0.40
b[a]	7.63	0.21	d	−12.45	5.2

[a] b is the mean over $2.3\,km\,s^{-1}$; c is the mean over $1.7\,km\,s^{-1}$

spacing was 36.6 km, giving a resolution of 1″.0 at 18 cm; the shortest spacing, 2.4 km, corresponds to a largest structure of 15″.5 still visible. On the second day, when observing the sources with large expansion velocities, only 9 telescopes could be used with a shortest baseline of 3.8 km (or 9″.8). The bandwidth on that day was 396 kHz, split into 128 channels, giving the same spectral resolution, but $N \simeq 0.04$ Jy per Hanning smoothed channel.

We used standard VLA reduction programs to produce small maps (32″ × 32″; cleaned 16″ × 16″) for each channel. For the weak emission part in the middle of the spectrum a number of channel maps were added to obtain a sufficient signal-to-noise ratio. This procedure provided us with 20–60 maps for each star. A selection of representative maps can be seen in Figs. 1–11. The contour values in these figures are 5, 10, ..., 95% of the strongest peak in

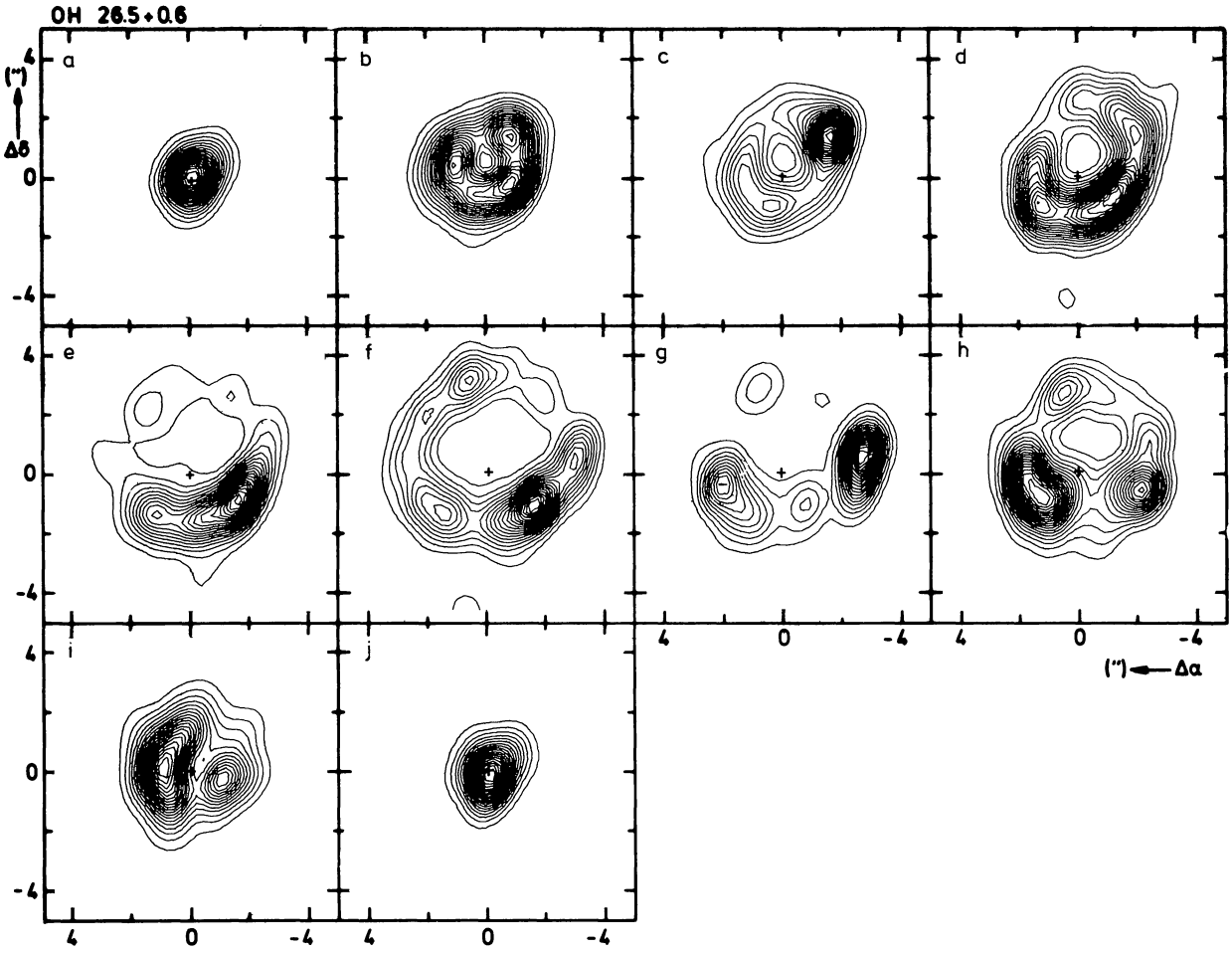

Fig. 5. OH 26.5 + 0.6, $v_{LSR} = +26.86\,km\,s^{-1}$, $v_e = 14.07\,km\,s^{-1}$, Total 58 maps

Map	Velocity ($km\,s^{-1}$)	Strongest peak (Jy)
a	14.52	263
b	12.23	15.4
c	9.93	14.3
d	7.63	2.9
e[a]	3.33	1.37
f[a]	− 2.41	1.01
g	− 7.29	6.2
h	− 9.59	5.6
i	−11.88	13.4
j	−14.18	104

[a] e und f are the mean over 5.2 $km\,s^{-1}$ (only for display purposes)

each map. The emission at the extreme velocities, displayed in the first and the last map of each source, has the shape of the theoretical synthesized beam profile, but is broadened by ~10%. We assumed it to be unresolved and used it as a measured synthesized beam.

Shortly after the VLA run all sources were observed with the Dwingeloo Radio Telescope as part of a much larger program, in which the 1612 MHz fluxes of 60 OH/IR stars are measured regularly (see Herman and Habing, 1984a). In this program it was established that most OH/IR stars are (very) long period variables with pulsation periods of up to 2000 days. From small time delays between different peaks in the line profile of one star, it appeared possible to determine the linear dimension of the circumstellar shell. In Table 1 the phases of the VLA and of the Dwingeloo single-dish observations can be found (columns 2 and 5), together with the integrated flux densities for the low- and high-velocity parts of the spectrum. The phases were calculated from the period and the time of maximum (corresponding to $\phi = 0$, while the time of minimum light corresponds to $\phi = 0.5$) in the radio light curve as found in the monitor program (Herman and Habing, 1984a). Parentheses indicate that the source is not variable, or that it only shows irregular, low amplitude variations. Columns 2, 3, and 4 are the VLA values, columns 5–7 the Dwingeloo measurements. Column 8 gives the percentage of the total flux detected at the VLA.

Generally, more than 80% of the total flux was seen in the VLA maps. Fluctuations on timescales of days to weeks as seen in the monitor program (Herman and Habing, 1984a) may account for 5–10% differences (see e.g. OH 28.5 − 0.0), as may the different methods of calibrating. We applied no bandpass correction, and assumed that the flux of 1741–038 was constant. We therefore conclude that (with the possible exceptions of OH 21.5 + 0.5,

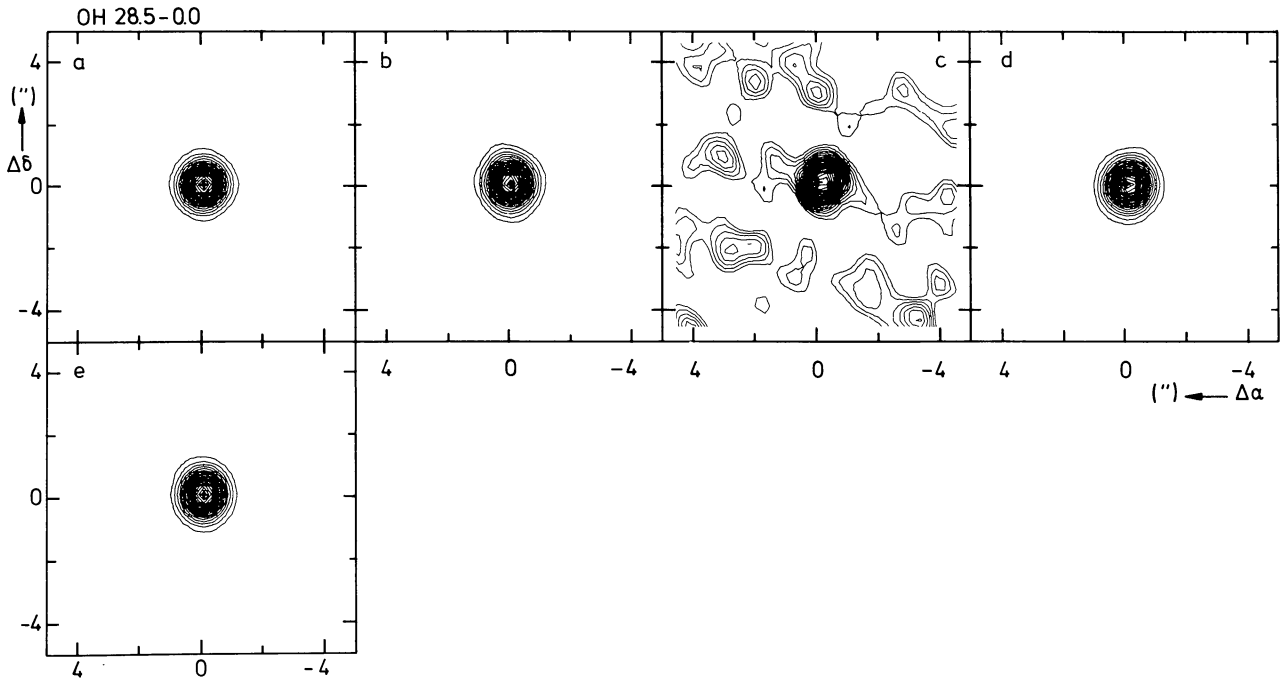

Fig. 6. OH 28.5 − 0.0, $v_{LSR} = +107.64\,km\,s^{-1}$, $v_e = 13.12\,km\,s^{-1}$, Total 26 maps

Map	Velocity ($km\,s^{-1}$)	Strongest peak (Jy)
a	13.09	11.1
b	9.64	2.1
c[a]	1.03	0.10
d	− 8.73	1.9
e	−12.74	7.2

[a] c is the mean over $11.5\,km\,s^{-1}$

OH 31.0 − 0.2, and OH 37.1 − 0.8) no significant part of the flux was missed, implying that the flux in all cases is confined to structures $< 8''$.

3. Data analysis

3.1. Positions and synthesized beam sizes

For a uniformly expanding shell the emission from the strongest maser peaks originates in the front and in the back caps of a narrow cone centered on the star (see Reid et al., 1977). We thus expect the peaks to coincide spatially and to be unresolved. In Table 2 the mean position of the low velocity (front) and high velocity (back) peak is listed. In all cases the peaks coincide within the uncertainty of 0.″13, except for OH 26.5 + 0.6 and OH 32.8 − 0.3. In the latter the high velocity peak shows two components, both displaced by ∼8″ with respect to the position of the low velocity peak.

The tabulated positions are in excellent agreement with previously determined values (cf. Bowers et al., 1981; Baud, 1981). We shall use the listed coordinates for the stellar positions (indicated by a cross in Figs. 1–11), taking the mean of the "front" and "back" position for OH 26.5 + 0.6 and the "front" position for OH 32.8 − 0.3.

The two strongest peaks of every star have a Gaussian brightness distribution (the high velocity peak of OH 32.8 − 0.3 excluded). They have the shape of the theoretical synthesized beam profile, deduced from the *U–V* coverage, but broadened by ∼10%. There are several reasons to assume that this broadening is not due to resolution of the peaks. In the first place the broadening increases with increasing distance from the phase calibrator 1741–038 (the only calibrator usable in this region of the sky). When we used a self calibration procedure, forcing the phase of the strongest feature to zero, this effect disappeared for the other peak. For our final maps self calibration was employed only for sources with $l > 30°$. In the second place we were troubled by some phase instabilities at dawn. A number of measurements around that time were rejected, but the remaining, lesser phase jumps might well explain the slight broadening with respect to the theoretical beam still present. In the further analysis we shall assume that the emission from the "front" and "back" sides of each star is unresolved and use these as a measure of the synthesized beam for deconvolution.

3.2. Shell sizes

Using a model of a uniformly expanding shell (see Reid et al., 1977), maps at different velocities with respect to the stellar velocity will be analysed in order to study the geometry of the shells. With such a model it is not only possible to determine the shell size, but also to investigate deviations from spherical symmetry. Because combining the phase lag radius (linear dimension along the line of sight) and the angular diameter yields

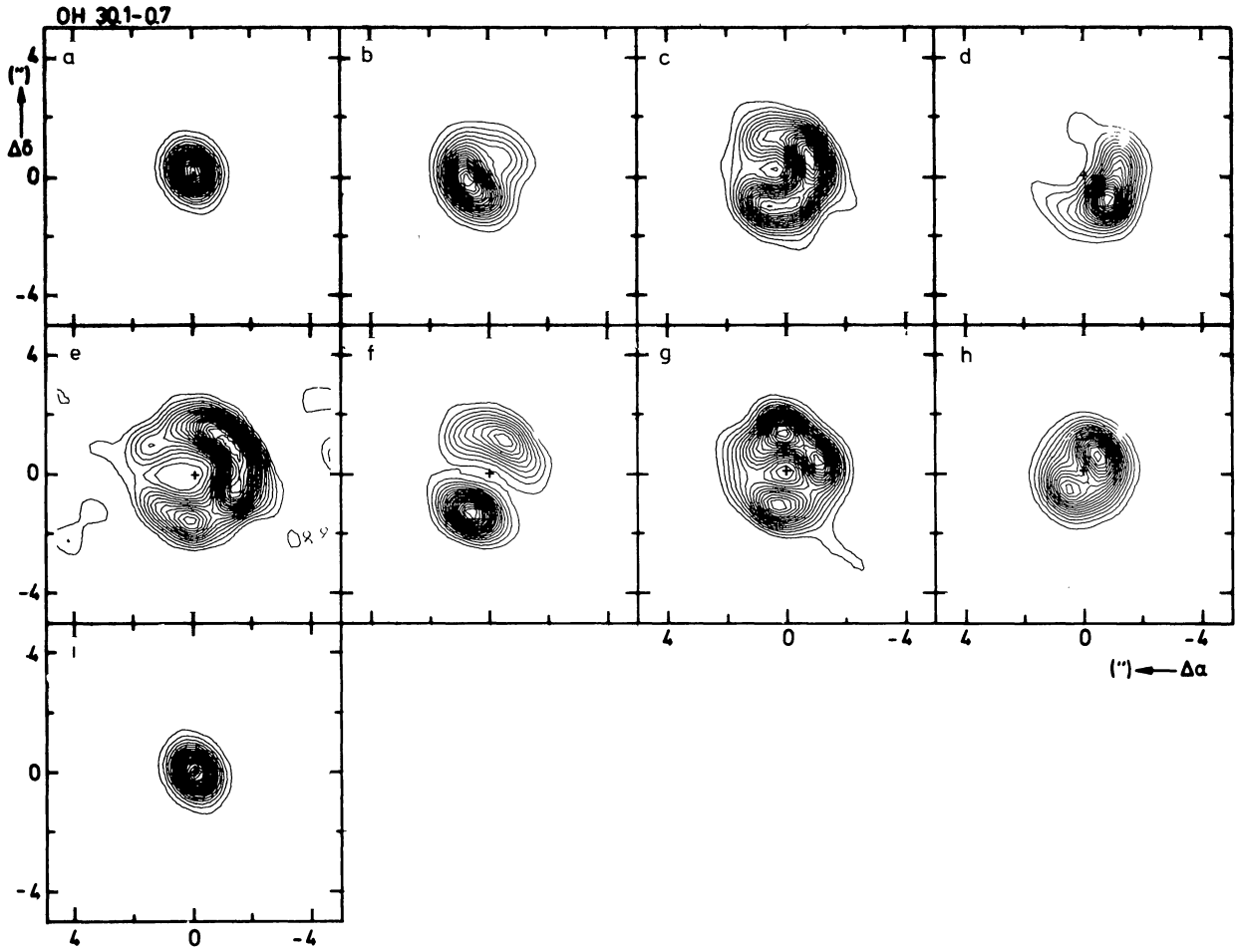

Fig. 7. OH 30.1 − 0.7, $v_{LSR} = +99.26\,km\,s^{-1}$, $v_e = 20.51\,km\,s^{-1}$, Total 46 maps

Map	Velocity ($km\,s^{-1}$)	Strongest peak (Jy)
a	20.38	41.5
b	16.93	3.8
c	13.49	1.3
d	10.05	2.3
e[a]	0.57	0.20

Map	Velocity ($km\,s^{-1}$)	Strongest peak (Jy)
f	−10.62	1.1
g	−13.49	1.8
h	−16.93	4.3
i	−20.95	40.7

[a] e is the mean over 12.1 $km\,s^{-1}$

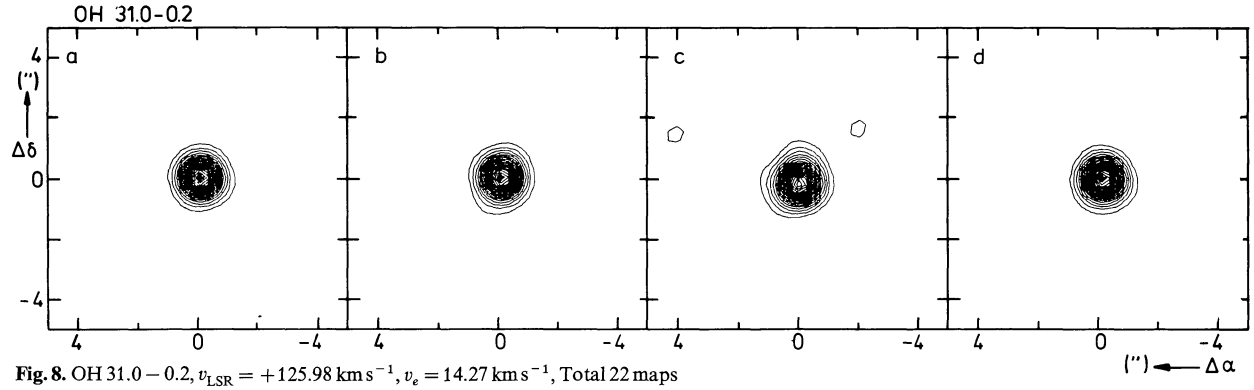

Fig. 8. OH 31.0 − 0.2, $v_{LSR} = +125.98\,km\,s^{-1}$, $v_e = 14.27\,km\,s^{-1}$, Total 22 maps

Map	Velocity ($km\,s^{-1}$)	Strongest peak (Jy)
a	14.35	5.9
b	11.48	2.8

Map	Velocity ($km\,s^{-1}$)	Strongest peak (Jy)
c	−11.48	1.2
d	−14.35	4.1

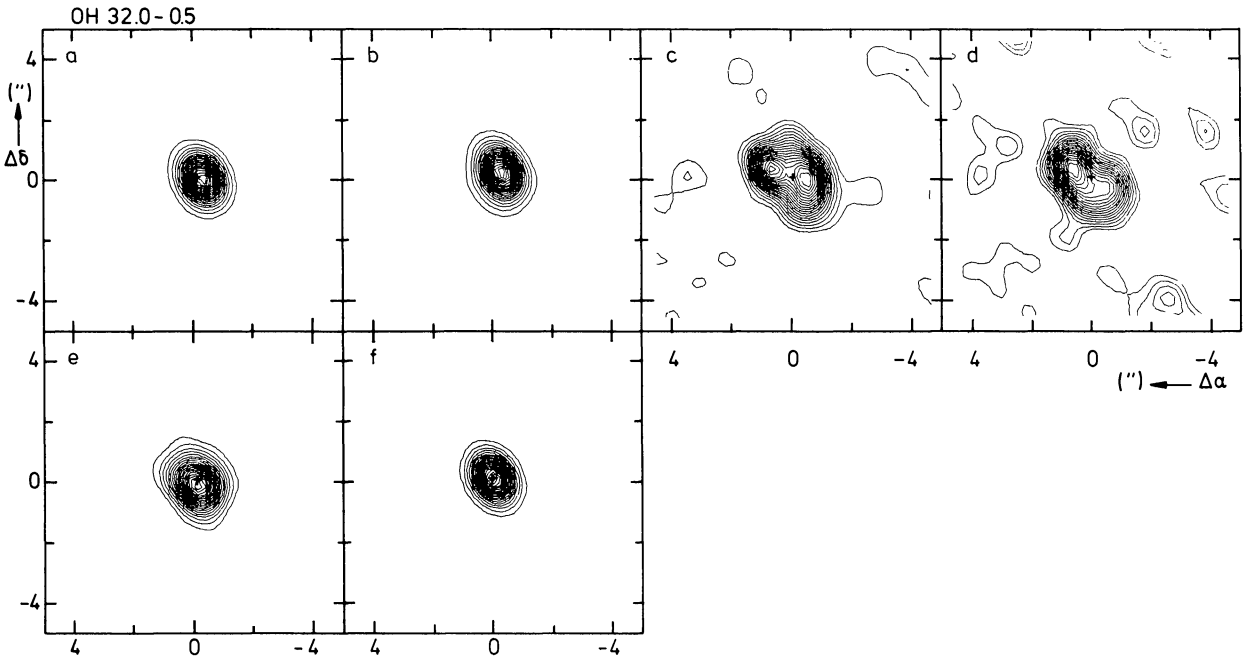

Fig. 9. OH 32.0 − 0.5, $v_{LSR} = +76.04\,km\,s^{-1}$, $v_e = 20.58\,km\,s^{-1}$, Total 28 maps

Map	Velocity ($km\,s^{-1}$)	Strongest peak (Jy)
a	20.09	6.8
b	18.37	2.8
c[a]	7.46	0.12
d[a]	− 5.45	0.12
e	−15.50	1.8
f	−20.66	9.6

[a] c is the mean over 16.1 $km\,s^{-1}$; d is the mean over 8.6 $km\,s^{-1}$

an accurate estimate of the distance to each individual object, such deviations are important to know.

Following Reid et al. (1977) we may write

$$a(v,\vartheta) = R_s(\vartheta)\left[1-\left(\frac{v}{v_e}\right)^2\right]^{1/2}. \quad (1)$$

Here $a(v,\vartheta)$ is the apparent angular radius of the shell at a radial velocity, v, with respect to the stellar radial velocity; v_e is the expansion velocity of the OH shell, and $R_s(\vartheta)$ is the radius at a position angle, ϑ. In the case of spherical symmetry R_s is independent of ϑ.

We measured $a(v,\vartheta)$ (in arcsec) by determining the position of the maximum emission with respect to the stellar position (α_0, δ_0: see Table 2) for 18 position angles ($\vartheta = 20°, 40°, \ldots, 360°$; see Fig. 12). For velocities close to the expansion velocity the two maxima in the crosscut are blended due to beam smearing (e.g. OH 26.5 + 0.6 for $v_e - 2.5\,km\,s^{-1} < v < v_e = 14.1\,km\,s^{-1}$; Fig. 5 between a and b, and between i and j). At these velocities we used for $a(v,\vartheta)$ half the full width at half maximum, deconvolved with the measured synthesized beam (see Fig. 13).

With the stellar velocity and v_e known from the single-dish line profiles (Herman and Habing, 1984a), Eq. (1) was solved for $R_s(\vartheta)$ using the method of least squares (Fig. 14). This could be done for the six resolved sources in our sample. The resulting values of $R_s(\vartheta)$ are shown in Fig. 15, and R_s, the average over all position angles, is given in Table 3a.

The five remaining objects (OH 18.5 + 1.4, OH 25.1 − 0.3, OH 28.5 − 0.0, OH 31.0 − 0.2, and OH 37.1 − 0.8) were not resolved. However, in all cases the position of the maximum emission around $v = 0$, where we expect the extent to be greatest, is shifted somewhat with respect to α_0, δ_0 (Fig. 16). If any of the resolved sources were at a larger distance, or intrinsically smaller, exactly the same situation would arise: only those places in the envelopes with enhanced emission would be seen.

To have at least an estimate of the shell diameter for these unresolved stars, we measured the distance of the maximum to the stellar position, $b(v)$ (in arcsec), in each channel map. The position angle of the maximum changes abruptly from channel to channel, suggesting that at some velocities we see one part, at others another part of the shell. Compare for example maps *b–d* of the resolved source OH 30.1–0.7 (Fig. 7), where the position angles of the strongest peak in each map differ considerably. We determined a radius, R_s, by a least squares fit to Eq. (1), substituting $b(v)$ for $a(v,\vartheta)$ and leaving out the ϑ dependence (Table 3b). We should bear in mind that the radii found in this way are presumably an *under*estimate of the true dimensions, because only the densest parts of the envelopes are seen.

4. Discussion

4.1. Asymmetry and thickness of the OH shells

It is clear from inspection of the individual channel maps (Figs. 1–11), that the brightness distribution is not uniform and the

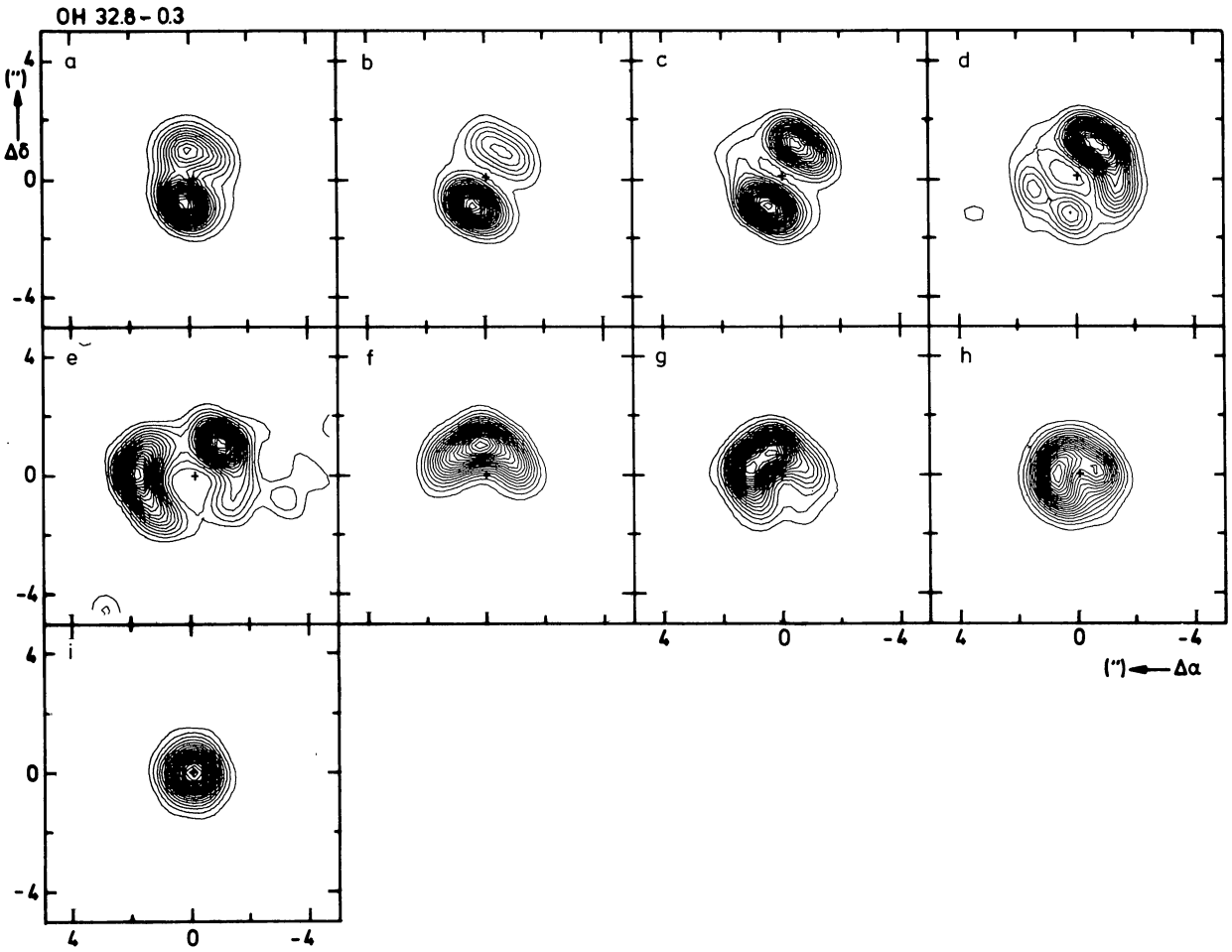

Fig. 10. OH 32.8 − 0.3, $v_{LSR} = +60.75\,km\,s^{-1}$, $v_e = 16.38\,km\,s^{-1}$, Total 32 maps

Map	Velocity ($km\,s^{-1}$)	Strongest peak (Jy)
a	15.15	5.7
b	14.01	4.7
c	12.86	1.8
d	11.71	1.5
e[a]	0.80	0.22
f	− 9.53	2.1
g	−11.82	2.3
h	−13.55	3.9
i	−15.27	14.0

[a] e is the mean over $17.2\,km\,s^{-1}$

angular extent not perfectly symmetric [4]. From the simple expanding shell model (see Reid et al., 1977) the flux, S, as a function of velocity is expected to behave as $S(v) \propto (v_d/v_e)\,[1-(v/v_e)^2]^{-1}$, where v_d is the Doppler width of the OH line. To analyse the deviations from this spherically symmetric model, we define

$$\Delta S(\vartheta) \equiv \log\left\{\sum_v S(v,\vartheta)\left[1-\left(\frac{v}{v_e}\right)^2\right]\left(\frac{v_e}{v_d}\right)\right\} - \log\bar{S}, \qquad (2)$$

a parameter that describes the velocity averaged deviations, at position angle ϑ, from the mean brightness $\bar{S}$. The measured peak fluxes $[S(v,\vartheta)]$ in the crosscuts are corrected for the projection onto the line of sight. The summation is taken only over those velocity maps which contained a well defined ring structure (e.g. for OH 26.5 + 0.6 over a velocity range of $25\,km\,s^{-1}$, deleting $2.5\,km\,s^{-1}$ on either side). By the summation over velocity any irregularities along the line of sight have been smoothed out. The Doppler width, v_d, is $0.58\,km\,s^{-1}$ for all sources (Herman and Habing, 1984a), and $\bar{S}$ is defined as

$$\bar{S} \equiv \frac{1}{18}\sum_{k=1}^{18}\left\{S(v,k\,20°)\left[1-\left(\frac{v}{v_e}\right)^2\right]\left(\frac{v_e}{v_d}\right)\right\}, \qquad (3)$$

where k is a running index ($k = 1, 2, \ldots, 18$), yielding the brightness, $S(v,\vartheta)$ for $\vartheta = 20°, 40°, \ldots, 360°$.

Similar to $\Delta S(\vartheta)$, we can define a parameter describing the deviations from the mean radius (R_s) at a position angle ϑ:

$$\Delta R_s(\vartheta) \equiv \log[R_s(\vartheta)] - \log[R_s], \qquad (4)$$

4 For OH 26.5 + 0.6, OH 30.1 − 0.7, and possibly OH 32.8 − 0.3 we might restore symmetry by changing the stellar position (Fig. 15). But for 26.5 + 0.6 this change would be 0″.65, so this is a rather unlikely hypothesis in view of the coincidence of the "front" and "back" peaks

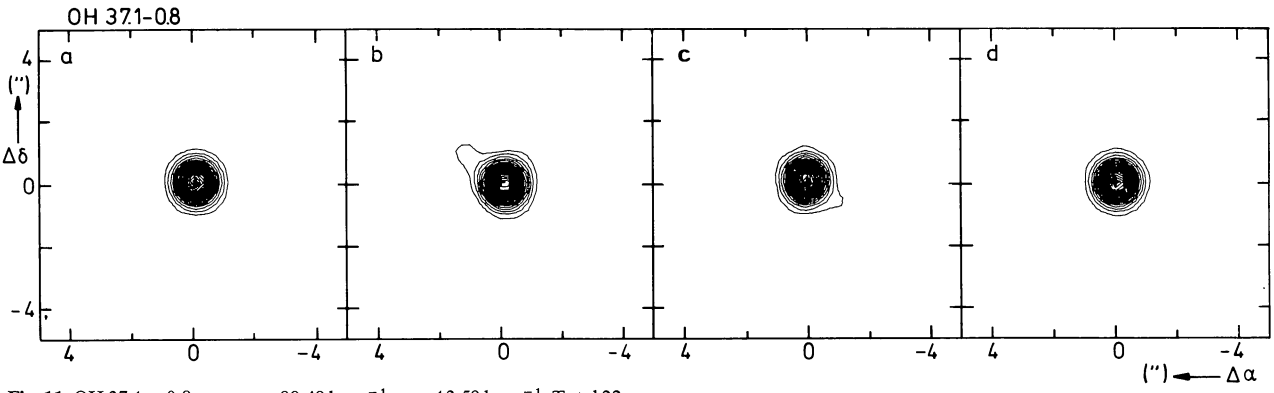

Fig. 11. OH 37.1 − 0.8, $v_{LSR} = +88.48\ km\ s^{-1}$, $v_e = 13.59\ km\ s^{-1}$, Total 22 maps

Map	Velocity ($km\ s^{-1}$)	Strongest peak (Jy)
a	13.26	13.6
b	9.24	1.5
c[a]	− 8.27	1.3
d	−12.00	10.2

[a] c is the mean over 1.1 $km\ s^{-1}$

Table 1

Name OH ———	φ VLA	S_{LV} (10^{-22} Wm^{-2})	S_{HV}	φ Dwing.	S_{LV} (10^{-22} Wm^{-2})	S_{HV}	%
(1)	(2)	(3)	(4)	(5)	(6)	(7)	(8)
18.5+1.4	0.915:	11.49	12.52	0.920:	11.91	12.47	98
20.7+0.1	0.001	16.39	10.89	0.007	16.26	15.74	85
21.5+0.5	0.546	15.06	11.77	0.550	24.89	17.70	63
25.1-0.3	0.795:	5.55	4.33	0.823:	6.22	6.29	79
26.5+0.6	0.130	272.0	466.3	0.138	362.2	616.6	75
28.5-0.0	0.107	15.53	14.67	0.112	13.40	13.27	113
30.1-0.7	0.854	96.02	96.26	0.860	111.4	122.2	82
31.0-0.2	(0.154)	6.26	8.88	(0.160)	9.89	12.97	66
32.0-0.5	0.001	26.39	11.84	0.006	31.91	16.48	79
32.8-0.3	0.317	58.84	28.73	0.320	73.79	38.81	78
37.1-0.8	(0.054)	13.21	13.47	(0.062)	18.88	19.91	69

Table 2

Name OH ———	α(1950.0) h m s	Δα s	δ(1950.0) o ' "	Δδ "	Remarks
18.5+1.4	18 16 47.370	.01	-12 09 27.30	.13	
20.7+0.1	18 25 44.320	.01	-10 52 50.85	.13	
21.5+0.5	18 25 45.490	.01	-10 00 12.40	.13	
25.1-0.3	18 35 33.360	.01	-07 12 34.65	.13	
26.5+0.6	18 34 52.470	.01	-05 26 37.15	.13	front
	.486	.01	36.90	.13	back
28.5-0.0	18 40 47.450	.01	-03 58 57.60	.13	
30.1-0.7	18 46 04.877	.01	-02 53 54.60	.13	
31.0-0.2	18 46 07.150	.01	-01 51 56.50	.13	
32.0-0.5	18 48 51.210	.01	-01 07 29.30	.13	
32.8-0.3	18 49 48.167	.01	-00 17 52.8	.13	front
	.150	.02	53.2	.75	back; shows structure
37.1-0.8	18 59 36.220	.01	+03 15 53.3	.13	

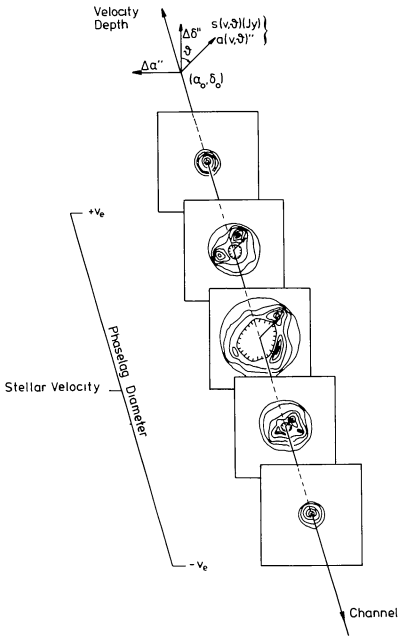

Fig. 12. Schematic representation of the location and the morphology of a thin shell for channel maps at various velocities, or depths, along the line of sight

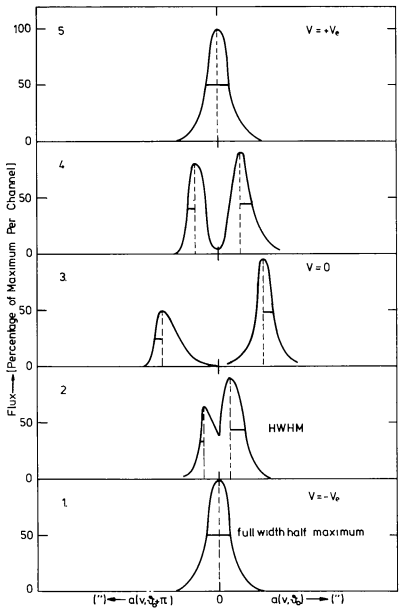

Fig. 13. Example of the measured crosscuts for an arbitrarily chosen direction ϑ. The numbers refer to the maps shown in Fig. 12

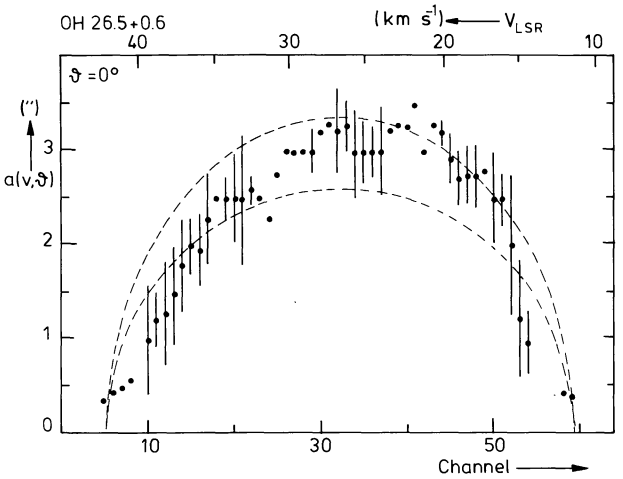

Fig. 14. Example of $a(v, \vartheta)$ as function of velocity for one cross direction ϑ. The bars indicate the full width at half maximum, deconvolved with the measured synthesized beam. They give an impression of the thickness of the shell. The dashed lines are curves of constant radius, R_s. They have been drawn at $R_s(\vartheta)$ $\pm$ m.e., the least squares solution to equation (1) $\pm$ the standard deviation

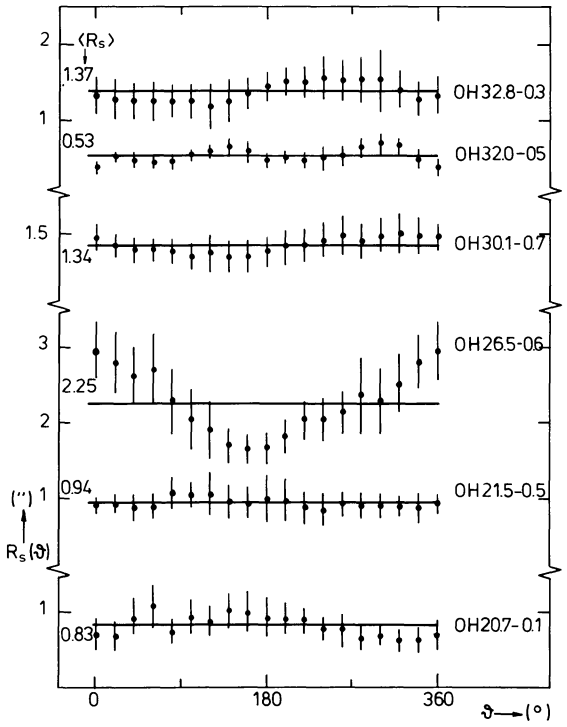

Fig. 15. Radius of the OH shell as function of cross direction for the resolved sources. The solid lines are the mean radii. The bars are the standard deviations (for individual measurements) of the measured $a(v, \vartheta)$ with respect to $R_s(\vartheta)$ $[1-(v/v_e)^2]^{0.5}$. They show the applicability of the model and are a measure for the thickness of the shells

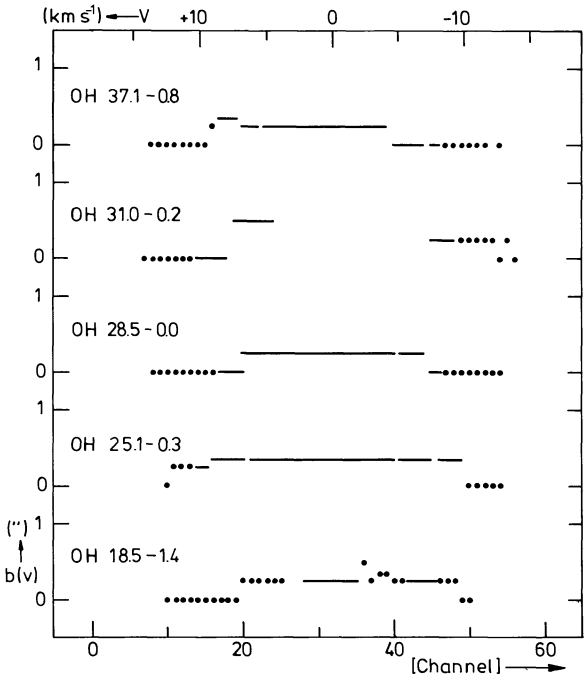

Fig. 16. Displacement of the maximum in the brightness distribution as function of velocity channel for the unresolved sources. Solid lines indicate that we took the average over a number of channels. Notice that these results are completely analogous to those for the resolved sources, when for the latter only the position of highest brightness in each map is considered. The uncertainty in $b(v)$ is $\sim 0''.1$ in each channel

where R_s is the mean of $R_s(\vartheta)$ [Eq. (1)] over ϑ. Figure 17 shows that $\Delta S(\vartheta)$ is roughly proportional to $\Delta R_s(\vartheta)^{-2}$ (line in Fig. 17). This result is based primarily on the measurements of OH 26.5 + 0.6, because these show the largest deviations, $\Delta S(\vartheta)$ and ΔR_s (cf. Fig. 15). Figure 17 shows that the stronger than average emission is always situated closest to the star. We expect (see Herman and Habing, 1984a) that for a given star $S_v(v) \propto f(v)\, n_{OH}\, R_{pump}$, where n_{OH} is the OH-density, R_{pump} is the net population transfer into the upper masing level and $f(v)$ is a function that describes the velocity dependence of the maser output. So one way to get brighter than average parts in the shell is "crowding in velocity space", i.e. a local enhancement of $f(v)$ because of a better velocity coherence from a larger part of the shell than expected from the model with uniform expansion. But from the extremely steep outer edges in all OH-spectra we can deduce that turbulent or streaming motions which could cause such a crowding are very small ($<0.2\,\mathrm{km\,s^{-1}}$; see Herman and Habing, 1984a). On the other hand we see coherent structures over much larger ranges in velocity, e.g. for OH 26.5 + 0.6 ($\vartheta = 45°$) from $v = 12.2$ to $7.6\,\mathrm{km\,s^{-1}}$ (Fig. 5b–5d). Therefore, velocity crowding as a mechanism to enhance the brightness locally can be excluded. The pump rate will be roughly constant throughout the shell of one star, as it depends on the number of far infrared photons emitted by the dust. Furthermore, the far infrared radiation field is determined by a much larger volume than are the local changes in OH brightness, because the shells are optically thin at 35 μm. The conclusion is that the brightness distribution reflects the density distribution of OH (see also Baud, 1981). Thus, the data in Fig. 17 provide the first direct observational evidence for a uniformly expanding shell with $n_{OH}(R) \propto R^{-2}$ at the distance from the star where the OH maser operates.

Next we compare the asymmetries as measured along the line of sight (in velocity) and perpendicular to it (in our VLA maps). Define δS_H, a parameter for the line of sight asymmetry

$$\delta S_H \equiv \log S_f - 0.5 \log(S_f S_b) = 0.5 \log(S_f / S_b), \qquad (5)$$

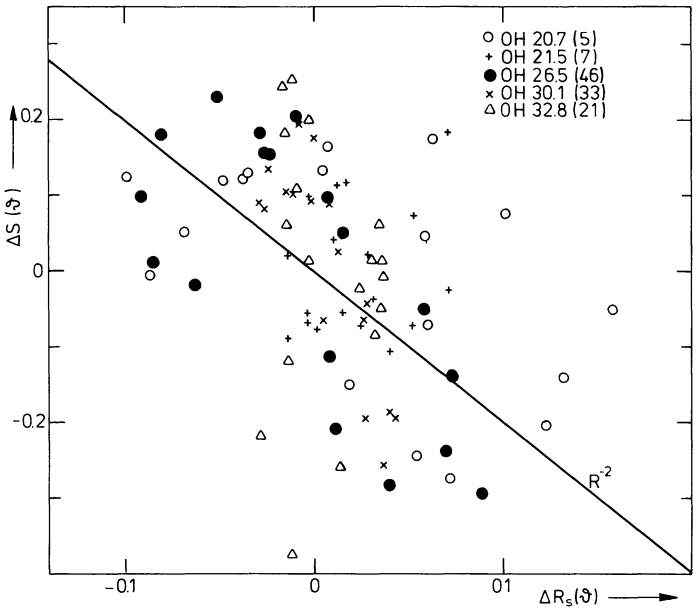

Fig. 17. Deviation of the flux, corrected for projection effects, as function of the deviation in radius from their mean values, measured for each cross direction ϑ. Between parentheses are the number of channel maps that could be used for each star. The solid line is not a fitted curve, but indicates a slope of -2. A least squares solution for OH 26.5 + 0.6 (the black dots), the only source that is both well resolved and has appreciable deviations from spherical symmetry, yields a slope of -2.09

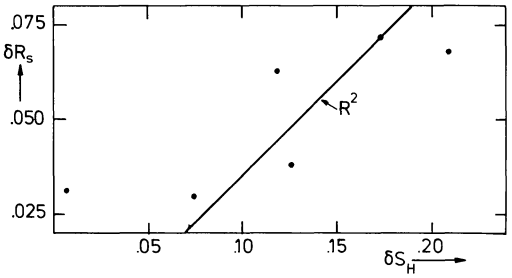

Fig. 18. Plot of the parameter δR_s, a measure of the asymmetry in the plane of the sky, against δS_H, which describes the asymmetry of the single-dish profile. Only the six resolved sources are shown

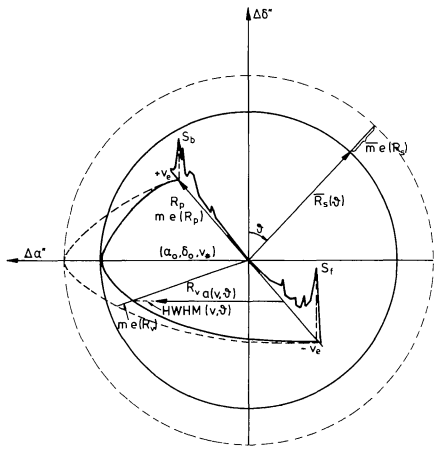

Fig. 19. Schematic representation of all measured quantities, as referred to in the text. The drawn and dashed circles are a cross section of the shell at the stellar velocity in the plane of the sky, and the profile lies along the line of sight. The stellar velocity, v_*, and the expansion velocity, v_e, are measured from the single-dish profiles, as are the peak flux densities, e.g. S_f and S_b. From the time delay between S_f and S_b (and interjacent peaks) a phase lag radius, R_p, can be derived. Maps at various velocities provide a measure of the apparent angular size, $a(v, \vartheta)$, and the thickness, HWHM (v, ϑ), of the shell for each cross direction, ϑ. Assuming a simple model, the apparent angular sizes may be converted to a radius of the shell, $R_s(\vartheta)$

where S_f and S_b are the flux densities of the front and back peak and $S_H = (S_f S_b)^{0.5}$ is their harmonic mean. This parameter is easily measured in the single-dish spectra. δS_H is compared with

$$\delta R_s \equiv \log\left[1 + \frac{\overline{\text{m.e.}(R_s)}}{R_s}\right], \tag{6}$$

where $\overline{\text{m.e.}(R_s)}$ is the mean error of $R_s(\vartheta)$ with respect to R_s and δR_s, which is nothing else than $\overline{\Delta R_s(\vartheta)}$, is a measure of perpendicular asymmetry. For the resolved sources roughly the same radial dependence as in Fig. 17 is found (Fig. 18). For the unresolved objects, however, the asymmetries in the plane of the sky, δR_s, seem to be much larger than expected from the ratio, δS_H, of the strongest peaks (see Table 3b). This conclusion needs to be supported by future observations using longer baselines (e.g. with MERLIN).

Another way to probe the asymmetry along the line of sight is to look at δR_v, the standard deviation with respect to $R_s(\vartheta)$, averaged over ϑ. In other words we smoothed over the irregularities in the plane of the sky [Eq. (1); Fig. 14]. Tables 3a and 3b show that δR_v is in reasonable agreement with δR_s and $0.5\,\delta S_H$, although it is systematically larger, probably because it is a convolution of the thickness and the deviations from symmetry of the shell.

Finally, the mean error, m.e. (R_p), in the determination of the "phase lag" radius (R_p; see Herman and Habing, 1984a) also reflects the asymmetry along the line of sight. Define

$$\delta R_p \equiv \log\left[1 + \frac{\text{m.e.}(R_p)}{R_p}\right], \tag{7}$$

which is for the resolved sources in very good agreement with δR_s (Table 3a). Only for OH 30.1 − 0.7 is δR_p substantially larger than all other asymmetry parameters; this is caused by two large phase lag deviations (see Herman and Habing, 1984a).

The five unresolved sources have, except for OH 28.5 − 0.0, at most small amplitude variations. When δR_p could be determined, it is in rough agreement with δR_s (Table 3b). Olnon et al. (1984) found that the infrared properties of these non-variable OH/IR stars also are markedly different. They are redder and have higher mass loss rates than the variable OH/IR stars.

Table 3a. The resolved sources

Name	$\overline{R_s(\theta)}$	$\overline{m.e(R_s)}$	δR_s	$m.e(R_v)$	δR_v	$\overline{HWHM}$	%	R_p	$me(R_p)$	δR_p	Log S_H	δS_H
OH ———	(")	(")	(a)	(")	(b)	(")		(10^{16}	cm.)	(b)	(Log Jy)	(b)
20.7+0.1	0.827	0.140	.068	0.195	.092	0.278	34	10.26	1.99	.077	0.938	.209
21.5+0.5	0.940	0.067	.030	0.197	.083	0.349	37	16.33	1.60	.041	1.318	.075
26.5+0.6	2.245	0.403	.072	0.343	.062	0.291	13	3.10	0.64	.082	2.440	.173
30.1-0.7	1.343	0.099	.031	0.204	.061	0.224	17	3.40	1.35	.145	1.798	.007
32.0-0.5	0.534	0.084	.063	0.096	.072	0.546:	102	7.47	1.52	.080	0.895	.119
32.8-0.3	1.369	0.125	.038	0.250	.073	0.260	19	11.52	1.13	.041	1.345	.124

Table 3b. The unresolved sources

Name	R_s	$m.e(R_s)$	δR_s	R_p	$m.e(R_p)$	δR_p	Log S_H	δS_H
OH———	(")	(")	(a)	(10^{16}	cm.)	(b)	(Log Jy)	(b)
18.5+1.4	0.255	0.154	.205	0.95	5.15:	.807	0.838	.097
25.1-0.3	0.362	0.187	.181	0.87	0.89	.306	0.861	.055
28.5-0.0	0.058	0.108	.457	0.17	2.14	1.132	1.028	.011
31.0-0.2	0.259	0.227	.273				0.811	.084
37.1-0.8	0.110	0.144	.364				1.169	.074

(a): parameter describing the asymmetry in the plane of the sky

(b): parameter describing the asymmetry along the line of sight

We can conclude the following: a) the asymmetry along the line of sight and perpendicular to it is almost equal for each individual star, and b) the flux ratio of the strongest peaks in a single-dish spectrum ("front" and "back" peak) is a good indication of the deviations from spherical symmetry in the envelope. As a result there is a natural limit of $\sim 10\%$ to the accuracy in the determination of the "phase lag" radii, when the simple spherically symmetric model is used.

The full width at half maximum (FWHM), measured for each velocity channel and in each crosscut ($=\vartheta$) (see Fig. 13), gives the thickness of the OH shell after deconvolution by the (measured) synthesized beam. The values found [see Table 3a: HWHM = 0.5 FWHM (v, ϑ)], appear to increase with decreasing apparent radius. This effect is probably instrumental, and hence the values of FWHM are only an uncertain indication of the shell thickness. Beam smearing causes this effect, although we tried to minimize its influence by measuring only the half width at the outside of the profiles and by computing the mean HWHM over the inner part of the velocity range. A second effect is that we added a number of channel maps around $v = 0$, thus slightly broadening the profiles, because we average over a (small) range in $a(v, \vartheta)$. Further, the values of FWHM are only marginally larger than the (measured) synthesized beam, so the deconvolution can introduce large errors. Only for stars where each channel could be treated separately, and for which $R_s(\vartheta) > 1''$, were the influences minor. Then we find an upper limit for the thickness of the OH shells of $< 0.2 R_s(\vartheta)$. This is in good agreement with the canonical value of $\sim 10^{16}$ cm for the thickness, as found from the phase lag measurements (Herman and Habing, 1984a).

4.2. Distances

By combining the phase lag radius (R_p), measured in cm, with the radius in the plane of the sky (R_s), measured in arcsec, we can determine the distance to each individual star

$$D(\text{kpc}) = 0.6695 \frac{R_p(10^{16}\,\text{cm})}{R_s(\text{arcsec})}, \tag{8}$$

where $R_s = \overline{R_s(\vartheta)}$. As was seen in the previous section, the values of R_p and R_s can be used directly, because to within the uncertainties ($\sim 10\%$) the asymmetries along the line of sight and perpendicular to it are equal. The resulting distances are given in Table 4, where some objects have been added with diameters known from literature (Norris et al., 1982; Baud, 1981). For the five unresolved sources the distances are given between parentheses, because the phase lag radii are very uncertain and the angular radius is probably underestimated. Columns 2–7 provide some relevant quantities, as found in the Dwingeloo program (Herman and Habing, 1984a). Column 2 gives the velocity with respect to the Local Standard of Rest, v_{LSR}, and column 3 the expansion velocity, v_e, of the shell. S_H is the harmonic mean of the mean flux density from the two strongest, low- and high-velocity, peaks (column 4) and Δm_r, defined as $2.5 \log (S_{max}/S_{min})$, is the amplitude of the radio light curve (column 5). The phase lag radius, R_{16} i.e. R_p in units of 10^{16} cm, and its uncertainty, ΔR_{16}, are given in columns 6 and 7. For the resolved sources the tabulated shell radius, R_s, is the mean over ϑ (column 8). The uncertainty in the shell radius, ΔR_s, is the standard deviation of the least squares solution of Eq. (1) averaged over ϑ (column 9). If the value for either R_{16}, due to small amplitude variations, or R_s, because the source is unresolved, is particularly uncertain, this is indicated by a colon next to the number. As a comparison to our calculated distances, D in column 10, the near and far kinematic distances are given (columns 12 and 13), based on the Schmidt mass model (Burton, 1974) and a distance to the galactic centre of $D_\odot = 9.2$ kpc (see next section). The uncertainties in the calculated distances, ΔD in column 11, are derived directly from ΔR_{16} and ΔR_s.

4.3. Distance to the galactic centre

One of the goals of our program was a direct determination of the distance to the galactic centre. Therefore, sources with large radial velocities were selected, which are expected to lie near their tangential points. But due to other restrictions (knowledge of position and time variability) some sources satisfy this criterion only marginally, or not at all. The velocity at the tangential point (v_T) is

$$v_T = \sin l \left[\Theta(R) \frac{D_\odot}{R} - \Theta(D_\odot) \right]. \tag{9}$$

Here R is the galacto-centric distance, $\Theta(R)$ the rotation velocity and $D_\odot$ the distance to the galactic centre. Denoting the

Table 4

Name OH ———	v_{LSR} (km s^{-1})	v_e (km s^{-1})	Log S_H (Log Jy)	Δm_r (mag)	R_{16} (10^{16} cm)	ΔR_{16}	R_s (")	ΔR_s (")		D (kpc)	ΔD (kpc)	D_{kin} (kpc) near	far
18.5+1.4	+176.17	10.85	0.838	0.19	0.95:	3.64	0.255:	0.029	u	(2.49:	9.54)	8.7	
20.7+0.1	+136.55	18.21	0.938	0.99	10.26	0.92	0.827	0.034		8.31	0.82	8.6	
21.5+0.5	+115.77	18.76	1.318	1.09	16.33	0.87	0.940	0.016		11.63	0.65	6.9	10.2
25.1-0.3	+142.88	12.14	0.861	0.21	0.87	0.63	0.362:	0.052	u	(1.61	1.19)	8.3	
26.5+0.6	+ 26.86	14.07	2.440	1.13	3.29	0.26	2.245	0.098		0.98	0.09	2.1	14.4
28.5-0.0	+107.65	13.12	1.028	0.77	0.17	1.51	0.058:	0.024	u	(1.96	1.35)	8.1	
30.1-0.7	+ 99.26	20.51	1.798	0.40	3.56	0.62	1.343	0.024		1.77	0.31	6.9	9.0
31.0-0.2	+125.98	14.27	0.811	0.13			0.259:	0.055	u			7.9	
32.0-0.5	+ 76.04	20.58	0.895	0.88	7.42	1.09	0.534	0.084		9.30	2.00	5.0	10.6
32.8-0.3	+ 60.75	16.38	1.345	1.24	16.46	0.33	1.369	0.030		8.05	0.24	4.0	11.4
37.1-0.8	+ 88.48	13.59	1.169	0.13			0.110:	0.032	u			6.9	7.8
39.7+1.5	+ 20.00	16.58	1.797	0.82	1.71	0.47	2.0 [a]	0.5		0.57	0.21	1.2	12.9
104.9+2.4	- 25.62	14.91	1.634	0.66	4.37	0.42	1.44[b]	0.02		2.03	0.20	2.3	
127.9-0.0	- 54.97	10.98	1.717	1.47	12.86	0.72	1.53[b]	0.02		5.63	0.32	3.9	
IRC+10011	+ 8.96	17.91	1.521	1.16	2.81	0.05	4. [c]	0.5:		0.47	0.06	0.5[d]	

[a] From Diamond *et al.*, in preparation

[b] From Norris *et al.*, 1982

[c] From Baud, 1981

[d] From Hyland *et al.*, 1972

u: unresolved at all velocities

uncertainty in the (geometric) distance by ΔD, we define a weight function

$$w \propto \left(\frac{v_{LSR}}{v_T}\right)^2 \left(\frac{D}{\Delta D}\right), \tag{10}$$

where we took $v_{LSR}/v_T = 1$, when $v_{LSR} \geqq v_T$; in other words: the greater the distance ambiguity, the less we believe our sources to follow the galactic rotation. The choice of these statistical weights is rather arbitrary, but this does not affect the result much. Taking in each case the kinematic distance that is closest to the value that we derived (taking the far distance for OH 21.5 + 0.5, OH 32.0 − 0.5, and OH 32.8 − 0.3), we find

$$\langle D - D_{kin} \rangle = \sum w^2 (D - D_{kin}) / \sum w^2 = 0.004\,(\text{kpc}). \tag{11}$$

$\langle D - D_{kin} \rangle$ is the (weighted) mean residual of the geometric distances, D, with respect to the kinematic distances, D_{kin} (calculated *assuming* $D_\odot = 9.2$ kpc). And thus is found

$$D_\odot = 9.2 \pm 1.2\,(\text{kpc}), \tag{12}$$

where the uncertainty is based solely on the standard deviation in Eq. (11). This is certainly not a spectacular improvement over existing results (e.g. Oort and Plaut, 1975 who find $D_\odot = 8.7 \pm 0.6$ kpc), but it shows that it is possible to determine $D_\odot$ in a very direct manner. The only assumption is that OH/IR stars generally follow the galactic rotation. Basically, this new result is based on five well resolved stars only, OH 20.7 + 0.1, OH 21.5 + 0.5, OH 30.1 − 0.7, OH 32.0 − 0.5, and OH 32.8 − 0.3. Of these five stars only the first three have $v_{LSR} \gtrsim v_T$. In view of the small number of stars no attempt was made to account for effects of the asymmetrical drift. Notice that the uncertainty given in Eq. (12) is a real, straightforward error of $D_\odot$. Oort and Plaut (1975) also give an internal error, but their value of $D_\odot$ depends on many stepping stones, which are needed to define the absolute mean magnitudes of RR Lyrae variables.

5. Conclusions

For the six sources in our sample that were resolved ($R_s > 0''.5$) we could determine distances with an accuracy of $\gtrsim 10\%$. Their mean distance from the Sun is 7.8 kpc. The OH shells have radii of $\sim 8\ 10^{16}$ cm and are fairly symmetric. It was found that the ratio of the two strongest peaks, front and back, in a single-dish line profile is a good indication of the degree of symmetry in the plane of the sky. The thickness is less than 20% of the radius, in reasonable agreement with the numerical value of $\sim 10^{16}$ cm as found by Herman and Habing (1984a). From the inhomogenities in the brightness distribution we could deduce that the density falls off as r^{-2} at large distances from the star.

The five unresolved sources all have small expansion velocities ($v_e < 15$ km s^{-1}) and only one, OH 28.5 − 0.0, shows appreciable time variations. Not only are the angular extents very small, but they also seem to be rather asymmetric. Hence no reliable distances could be found for these sources. If their mean distance from the Sun is the same as for the resolved sources, their intrinsic shell dimension is a factor 5 smaller on the average. Olnon et al. (1984) found that this class of OH/IR stars is also notably different in the infrared. All these characteristics suggest that these stars are the most extreme members of the OH/IR star population and they have perhaps already left the asymptotic giant branch towards planetary nebula formation.

By comparing geometrically determined distances with kinematic distances the galactic distance scale could be set in a very direct manner. It was found that $D_\odot = 9.2 \pm 1.2$ kpc. An increase of the limited number of objects for which geometric distances are available, will improve this determination to a far better accuracy than that of any other method.

Acknowledgements. We wish to thank the VLA staff for their continuous assistance with observations and reduction. Dr. M.H.

Schneps helped us with a number of valuable comments and Dr. N. Douglas with his thorough reading of the manuscript. J. Herman was supported by a grant from ASTRON, the Netherlands Foundation for Astronomical Research. ASTRON receives its funds from ZWO, the Netherlands Organization for the Advancement of Pure Research.

References

Baud, B.: 1981, *Astrophys. J. Letters* **250**, L79
Benson, J.M., Mutel, R.L.: 1979, *Astrophys. J.* **233**, 119
Bidelman, W.P.: 1980, *Publ. Warner Swasey Obs., Case Western Reserve Univ.*, Vol **2**, No. 6, p. 185
Booth, R.S., Kus, A.J., Norris, R.P., Porter, N.D.: 1981, *Nature* **290**, 382
Bowers, P.F., Johnston, K.J., Spencer, J.H.: 1981, *Nature* **291**, 382
Bowers, P.F., Reid, M.J., Johnston, K.J., Spencer, J.H., Moran, J.M.: 1980, *Astrophys. J.* **242**, 1088
Burton, W.B.: 1974, in *Galactic and Extra Galactic Astronomy*, eds. G.L. Verschuur, K.J. Kellerman, p. 82
Engels, D.: 1979, *Astron. Astrophys. Suppl.* **36**, 337
Herman, J.: 1983, The Nature of OH/IR Stars, Ph.D. thesis, RUL
Herman, J., Habing, H.J.: 1984a, *Astron. Astrophys.* (submitted, see Herman, J. 1983, Chap. II)
Herman, J., Habing, H.J.: 1984b (in preparation, see Herman, J., 1983, Chap. V)
Hyland, A.R., Becklin, E.E., Frogel, J.A., Neugebauer, G.: 1972, *Astron. Astrophys.* **16**, 204
Jones, T.J., Hyland, A.R., Wood, P.R., Gatley, I.: 1983, *Astrophys. J.* **273**, 669
Masheder, M.R.W., Booth, R.S., Davies, R.D.: 1974, *Monthly Notices Roy Astron. Soc.* **166**, 561
Neugebauer, G., Leighton, R.B.: 1969, Two Micron Sky Survey, NASA SP-3047
Norris, R.P., Diamond, P.J., Booth, R.S.: 1982, *Nature* **299**, 131
Olnon, F.M., Baud, B., Habing, H.J., de Jong, T., Harris, S., Pottasch, S.R.: 1984, *Astrophys. J. Letters*, **278**, L41
Oort, J.H., Plaut, L.: 1975, *Astron. Astrophys.* **41**, 71
Reid, M.J., Muhlemann, D.O., Moran, J.M., Johnston, K.J., Schwartz, P.R.: 1977, *Astrophys. J.* **214**, 60
Thompson, A.R., Clark, B.G., Wade, C.M., Napier, P.J.: 1980, *Astrophys. J. Suppl.* **44**, 151